Journal of Superconductivity and Novel Magnetism (2019) 32:893–901
https://doi.org/10.1007/s10948-018-4734-4

ORIGINAL PAPER

Effect of the Boron Content on the Amorphization Process and Magnetic Properties of the Mechanically Alloyed $Fe_{92-x}Nb_8B_x$ Powders

T. Chabi[1] · N. Bensebaa[1] · S. Alleg[1] · S. Azzaza[1] · J. J. Suñol[2] · E. K. Hlil[3]

Received: 26 April 2018 / Accepted: 12 May 2018 / Published online: 15 June 2018

Abstract

The effect of the B content on the microstructural, structural, and magnetic properties of partially amorphous $Fe_{92-x}Nb_8B_x$ ($x = 5$, 10, 15, and 20) alloys has been investigated by means of scanning electron microscopy, X-ray diffraction, high and low-temperature extraction-type magnetometers. The XRD results reveal the formation of a nanocomposite structure where nanocrystalline bcc α-Fe and Fe_2B phases are embedded into an amorphous matrix. The FeB boride is observed for higher boron contents ($x = 15$ and 20), and the crystallite sizes are in the range of 7–24 nm. As the B content increases, the amorphous phase-relative proportion and coercivity increase, whereas the saturation magnetization decreases. An important magnetic hardening occurs by lowering the temperature from 400 to 5 K for $x = 20\%$ B. The variation of the Curie temperature can be attributed to the heterogeneity of the amorphous matrix.

Keywords Nanocrystalline materials · Mechanical alloying · Fe-Nb-B alloys · X-ray diffraction · Magnetic properties

1 Introduction

Mechanical alloying (MA) or high-energy ball milling (HEBM) is one of the various techniques used to synthesize nanocrystalline (NC) materials. It is a powder metallurgy method where the starting elemental or prealloyed powders are subjected to a high-speed deformation mechanism (10^3 to 10^{-3} s^{-1}) by heavy plastic deformation, fracture, cold welding, rewelding, and agglomeration. The final product is achieved by controlling several parameters which are related to each other such as the ball mill type, milling time, milling temperature, ball-to-powder weight ratio (BPR), rotation speed, process control agent, grinding media (balls, material, volume of the vial, etc.), and milling atmosphere. HEBM has proved its suitability and availability as one of the powerful and simple techniques for producing amorphous alloys, nanostructured materials, solid solutions, and intermetallics [1–10].

The FeMB alloys (M = Zr, Hf, Nb) or Nanoperm, which contain around 80% of iron, 7% of transition metals (Zr, Hf, Nb), and 13% of boron, are structurally and magnetically biphasic since they are composed of hard ferromagnetic nanograins dispersed homogeneously into a soft ferromagnetic amorphous matrix [11]. These materials are very interesting due to their soft magnetic properties such as effective permeability and saturation magnetic flux density [12–15]. Consequently, they can be used in many industrial applications such as telecommunications, power electronics, microdevices, generators, and sensors. The augmentation of both B and Nb percentages in the Fe-based amorphous alloys plays a main role in the thermal stability [10]. The outcome is that the nanocrystallization takes place in the form of pure iron crystals which favor a high saturation induction (1.5–1.7 T) and a Curie temperature (T_C) close to 769 °C. Furthermore, Nanoperm alloys lose their magnetization with the formation of borides [16]. Among the Nanoperm alloys, the ternary Fe-Nb-B system has attracted much attention, owing to its useful properties [17–19], and has been prepared in ribbon form by melt

✉ S. Alleg
safia.alleg@univ-annaba.dz

[1] Laboratoire de Magnétisme et Spectroscopie des Solides (LM2S), Département de Physique, Université Badji Mokhtar Annaba, BP 12, 23000 Annaba, Algeria

[2] Departament De Fisica, Universitat de Girona, Campus Montilivi, 17071 Girona, Spain

[3] Institut NEEL, CNRS, Université Grenoble Alpes, 25 Rue des Martyrs BP 166, 38042 Grenoble Cedex 9, France

spinning [20] and planar flow casting [21], bulk form by arc melting [15], and powder form by MA [18]. Depending on the B content, it has been reported that the end product consists, generally, of a mixture of bcc α-Fe, borides, and amorphous phases [22]. In the ball-milled $Fe_{94-x}Nb_6B_x$ (x = 9, 14, 20) alloys, it has been found that the Fe lattice parameter increases with increasing B content while the crystallite size decreases [23] and the boron atoms segregate at the grain boundaries [7]. The $Fe_{65+x}Nb_{10}B_{25-x}$ (x = 0, 5, 10) metallic glasses prepared by arc melting exhibit soft magnetic properties in the glassy state, and their nanocrystallization leads to the enhancement of the coercivity [24]. A mixture of α-Fe, Nb(B), and highly disordered Fe(Nb, B) solid solution has been obtained in the mechanically alloyed $Fe_{62}Nb_8B_{30}$ powders for 25 h, while the paramagnetic amorphous structure is achieved on further milling time [18]. It is obvious that the preparation conditions influence the end product and the properties of the mechanically alloyed powders. Consequently, the aim of the present work is to study the effect of boron content on the amorphization process and on the structural, microstructural, morphological, and magnetic properties of the ball-milled $Fe_{92-x}Nb_8B_x$ (x = 5, 10, 15, and 20) powders. An accurate quantitative phase analysis (QPA) was used to determine the amorphous phase-relative proportion by using the MAUD program [25].

2 Experimental Details

$Fe_{92-x}Nb_8B_x$ (x = 5, 10, 15, and 20) powder mixtures were mechanically alloyed for 50 h from pure elemental powders of Fe (6–8 µm, 99.7%), Nb (74 µm, 99.85%), and amorphous B (>99%). The milling process was performed in a planetary ball mill Retsch PM400 under an argon atmosphere using hardened steel vials and balls. The ball-to-powder weight ratio was about 7:1, and the rotation speed was 700 rpm. In order to

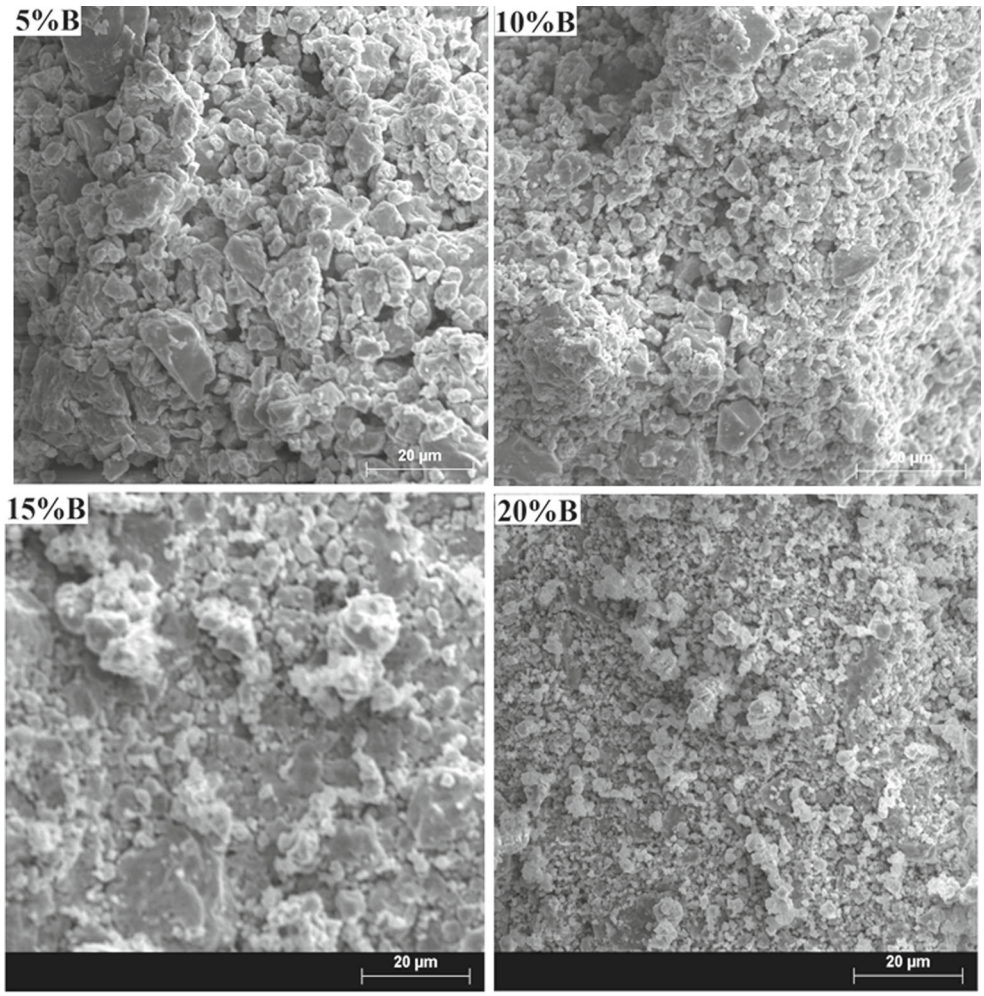

Fig. 1 SEM micrographs of $Fe_{92-x}Nb_8B_x$ powders

avoid the excessive increase of the temperature inside the vials, the milling process was interrupted each at 1/2 h for 1/4 h. Morphological changes of the powder particles were followed by scanning electron microscopy (SEM) in Zeiss DSM960A apparatus. The structural evolution was investigated by X-ray diffraction (XRD) by means of PANanalytical Empyrean diffractometer in a (θ–θ) Bragg-Brentano geometry with Co-Kα radiation ($\lambda_{Co} = 1.78901$ Å). Phase identification, lattice parameters (a, c), average crystallite size ($<L>$), root mean square (rms) strains ($<\sigma^2>^{1/2}$), phase-relative proportion, atomic positions, etc., were obtained from the refinement of the XRD patterns by the MAUD program which is based on the Rietveld method [26] combined with Fourier analysis

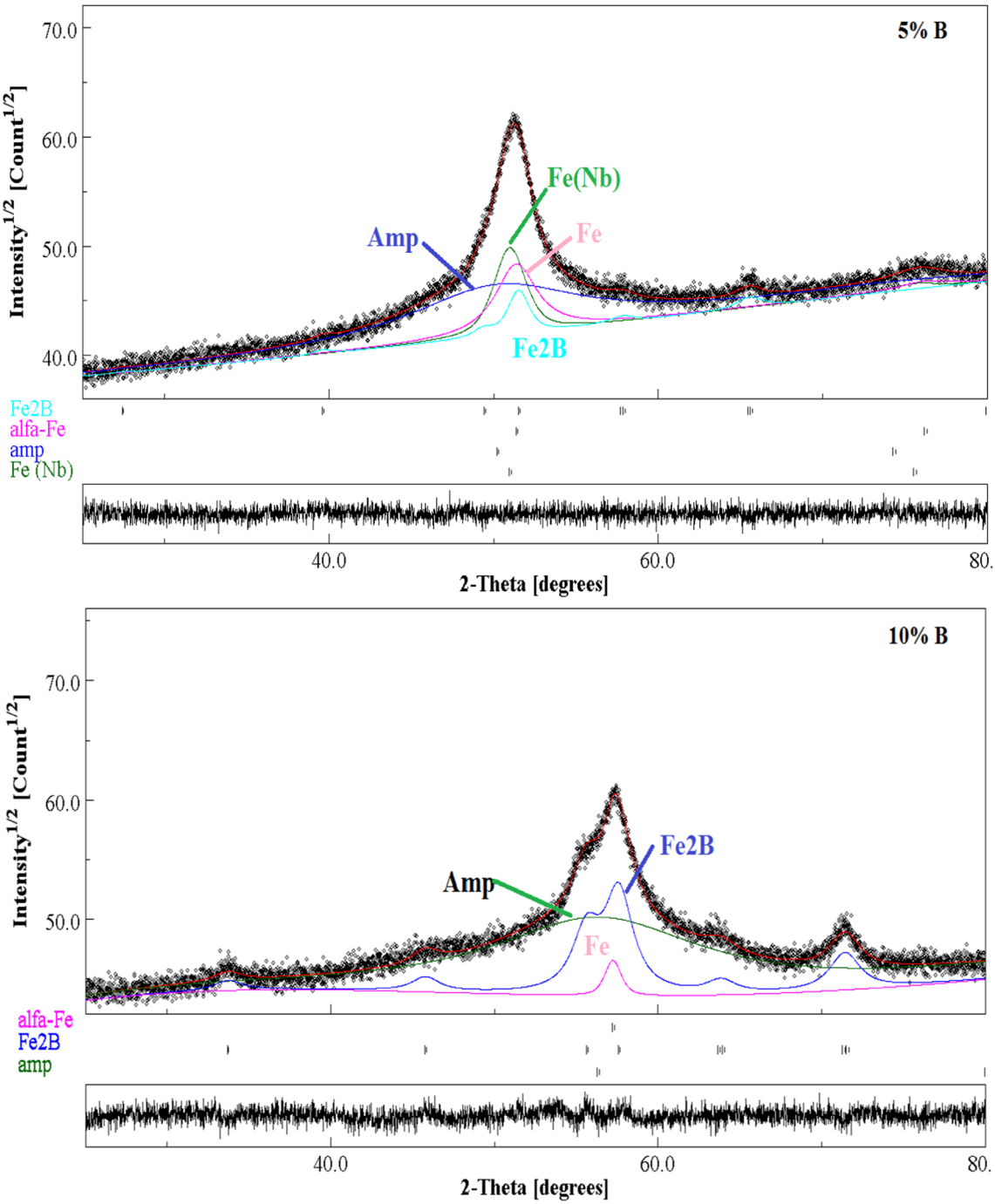

Fig. 2 Rietveld refinement of the XRD patterns of $Fe_{92-x}Nb_8B_x$ powders

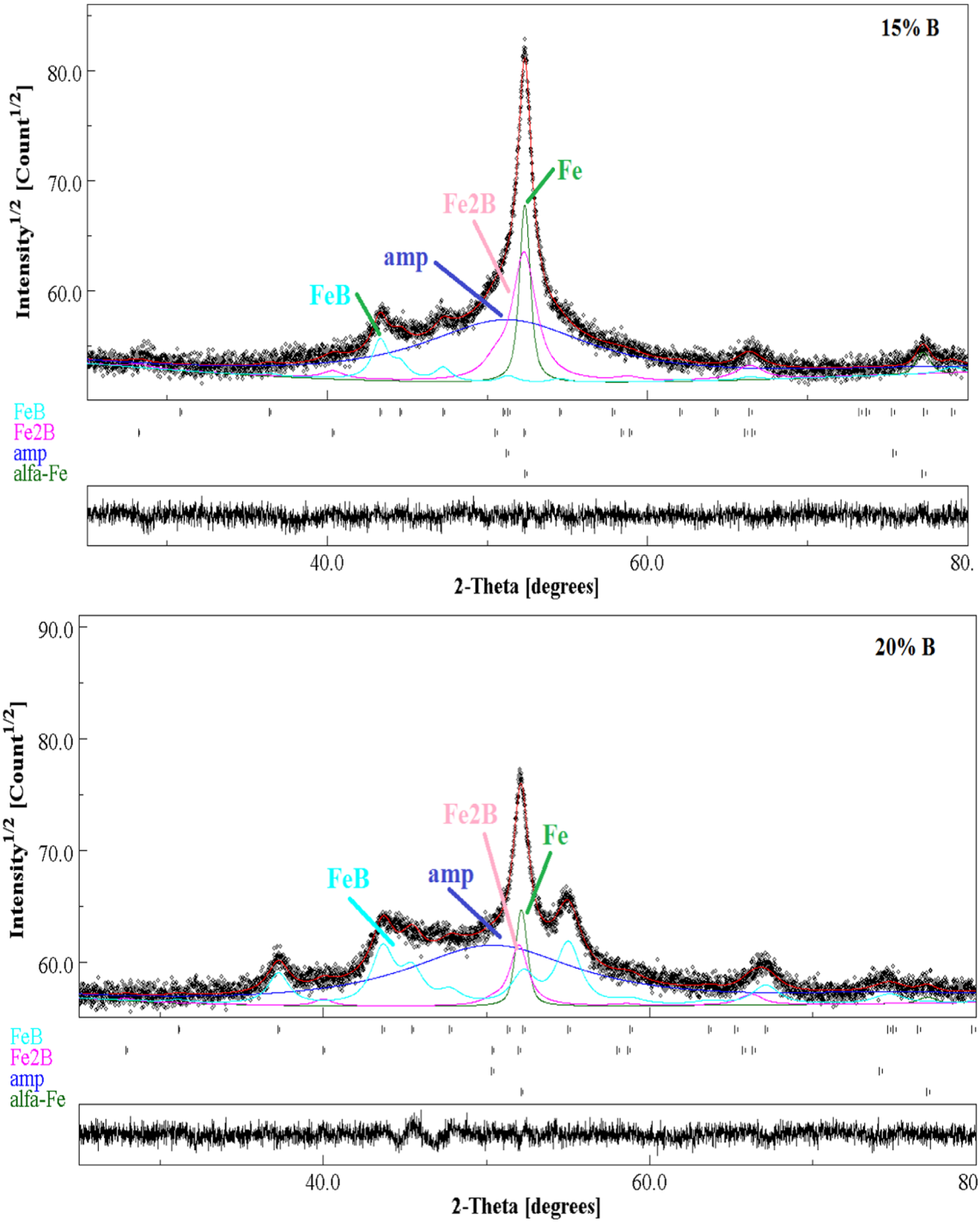

Fig. 2 (continued)

which is well adapted for disordered alloys. The saturation magnetization, coercivity, saturation-to-remanence ratio, and Curie temperatures were determined by measuring $M(H)$ hysteresis loops and $M(T)$ curves using the BS1 and BS2 extraction-type magnetometers developed at Néel Institute (http://neel.cnrs.fr/) for high and low temperatures, respectively.

3 Results and Discussion

3.1 Morphological Evolution

The powder particles are subjected to flatting, fracturing, cold welding, and rewelding during the milling process. Consequently, the formed fresh surfaces show a high

activity which results in strong bonding between the hard phases and the metallic matrix. Figure 1 displays the morphological changes of the ball-milled $Fe_{92-x}Nb_8B_x$ (x = 5, 10, 15, and 20) powders for 50 h. One observes that the powder morphologies are different from each other. The ductile particles are flattened by the compressive forces due to the collision of the balls inside the vials, while the brittle particles (boron) are fractured and welded. Hence, the microforging process causes a change in the shape of the individual particles. The existence of bigger and smaller particles results from the competition between fracturing and cold welding. For 20% B, the important microstructural refinement can be related to the domination of the fracturing process since the boron element is hard and brittle.

3.2 Phase Formation

Figure 2 illustrates the evolution of the XRD patterns of the $Fe_{92-x}Nb_8B_x$ alloys as a function of B content. The widening of the diffraction peaks and the reduction of their intensities are related to the decrease of the crystallite size and the increase of the internal level strains. In addition to the broad amorphous halo (located at about $2\theta = 52°$), sharp diffraction peaks linked to NC α-Fe and Fe_2B phases are observed. For 15% B and 20% B samples, one notes also the appearance of new diffraction peaks related to the formation of the FeB boride. Accordingly, the Rietveld refinements of the XRD patterns were performed by introducing either three or four phases among the following structures: bcc α-Fe (space group *Im3m*, lattice parameter $a_0 = 0.2866$ nm), tetragonal Fe_2B boride (space group *I4/mcm*, lattice parameters $a_0 = 0.511$ nm and $c_0 = 0.4249$ nm), orthorhombic FeB (space group *Pbnm:cab*, lattice parameters $a_0 = 0.4053$ nm, $b_0 = 0.5495$ nm, and $c_0 = 0.2946$ nm), and amorphous phase. This later was quantified according to the Le Bail model [25] by keeping $<L> = 1$ nm and $<\sigma^2>^{1/2} = 0$. The obtained results are summarized in Table 1.

The presence of the metalloid B in the Fe-Nb-B alloys obstructs coarsening of the bcc grains, enhances the glass forming ability (GFA), provides good magnetic properties, and gives a better thermal stability of the residual amorphous phase [27]. Moreover, the formation of the amorphous phase in the mechanically alloyed Fe-Nb-B system can be related to the important amount of structural defects and impurity atoms in the interstitial sites which distorted locally the crystal lattice. Consequently, the interdiffusion between the elemental powders is accelerated and the free energy of the crystalline phases is enlarged compared to the free energy of the amorphous ones, leading to an atomic disorder and facilitating the amorphization process. Furthermore, the packed local structure is favored by the segregation of boron inclusions at the grain boundaries, the stronger attractive interaction between Fe and B atoms, as well as the presence of three elements (Fe, Nb, and B) with a significant difference in atomic size ratios ($r_{Nb} = 0.198$ nm $> r_{Fe} = 0.124$ nm $> r_B = 0.087$ nm). When the local atomic strains generated by size differences between B, Nb, and Fe attain a critical level, the local atomic coordination number changes and the topological instability of the crystalline lattice lead to the formation of the amorphous phase. This later occurs at the Fe/B, Fe/Nb, and

Table 1 Lattice parameters (a, b, and c), crystallite size ($<L>$), microstrains ($<\sigma^2>^{1/2}$), and relative proportions of the ball-milled $Fe_{92-x}Nb_8B_x$ (x = 5, 10, 15, and 20) powders for 50 h

Sample	Phase	a (nm) ± 10^{-4}	Δa (%)	b (nm) ± 10^{-4}	Δb (%)	c (nm) ± 10^{-4}	Δc (%)	$<L>$(nm) ± 2	$<\sigma^2>^{1/2}$ ± 10^{-3}	Proportions (%)
5% B	α-Fe	0.2867	0.04	–	–	–	–	07	0.625	16.0
	Fe (B)	0.2899	1.15	–	–	–	–	12	1.321	24.0
	Fe_2B	0.5162	1.02	–	–	0.4205	−1.03	08	0.394	12.4
	Amorphous	–	–	–	–	–	–	–	–	47.6
10% B	α-Fe	0.2867	0.04	–	–	–	–	20	0.392	06.4
	Fe_2B	0.5169	1.15	–	–	0.4198	−1.20	08	0.263	38.9
	Amorphous	–	–	–	–	–	–	–	–	54.7
15% B	α-Fe	0.2868	0.07	–	–	–	–	23	0.285	29.3
	Fe_2B	0.5173	1.23	–	–	0.4194	−1.29	08	0.988	09.6
	FeB	0.4080	0.66	0.5709	3.89	0.3040	3.19	10	0.245	04.9
	Amorphous	–	–	–	–	–	–	–	–	56.2
20% B	α-Fe	0.2867	0.04	–	–	–	–	24	0.323	06.9
	Fe_2B	0.5208	1.20	–	–	0.4175	−1.74	09	0.174	09.7
	FeB	0.4137	2.07	0.5577	1.49	0.2972	0.88	11	0.431	17.4
	Amorphous	–	–	–	–	–	–	–	–	66.0

Nb/B interfaces, and the mixing of the elemental powders at the atomic level is favored by the high negative heats of mixing which are of about −26, −16, and −54 kJ/mol for Fe-B, Nb-Fe, and Nb-B [28], respectively. Furthermore, the formation of the amorphous phase can be accelerated by the increase of the boron content. Indeed, in the Fe-based alloys with less than 12 at.% B, a metastable bcc Fe(B)-supersaturated solid solution was obtained instead of an amorphous phase [18, 29].

The formation of Fe_2B and FeB iron borides can be attributed to the reaction between Fe and B with similar diffusion coefficients [30] as well as the excess of boron content which is introduced into the Fe matrix during the milling process, although its solubility is less than 0.02 wt% at room temperature [31]. Besides, the diffusivity of solute elements into the iron matrix might be enhanced by the presence of a variety of crystal defects (dislocations, vacancies, stacking faults, and grain boundaries) that are introduced by the heavy plastic deformation into the powder particles. Consequently, the refined microstructural features decrease the diffusion distances and the slight increase in temperature during the milling process helps the diffusion process, leading to the formation of intermetallic compounds. According to the binary Fe-B-phase diagram [31], Fe_2B and FeB boride phases can be formed at the thermodynamic equilibrium with a B content of about 8.8 and 16 wt%, respectively.

The crystallite size of the obtained phases varies between 7 and 24 nm. One notes that the α-Fe crystallite size increases as a function of B content (Table 1), while that of the Fe_2B phase remains constant. The relative proportion of Fe_2B phase increases to 38.9% for 10% B, decreases for 15% B, and levels off. This decrease might be correlated to the segregation of B atoms in the grain boundaries. Such particular behavior might be ascribed to the instability of the segregation process, and its effect can be inhibited beyond this critical concentration. Similar comportment was observed in the $Fe_{60}Al_{40-x}B_x$ alloys [32].

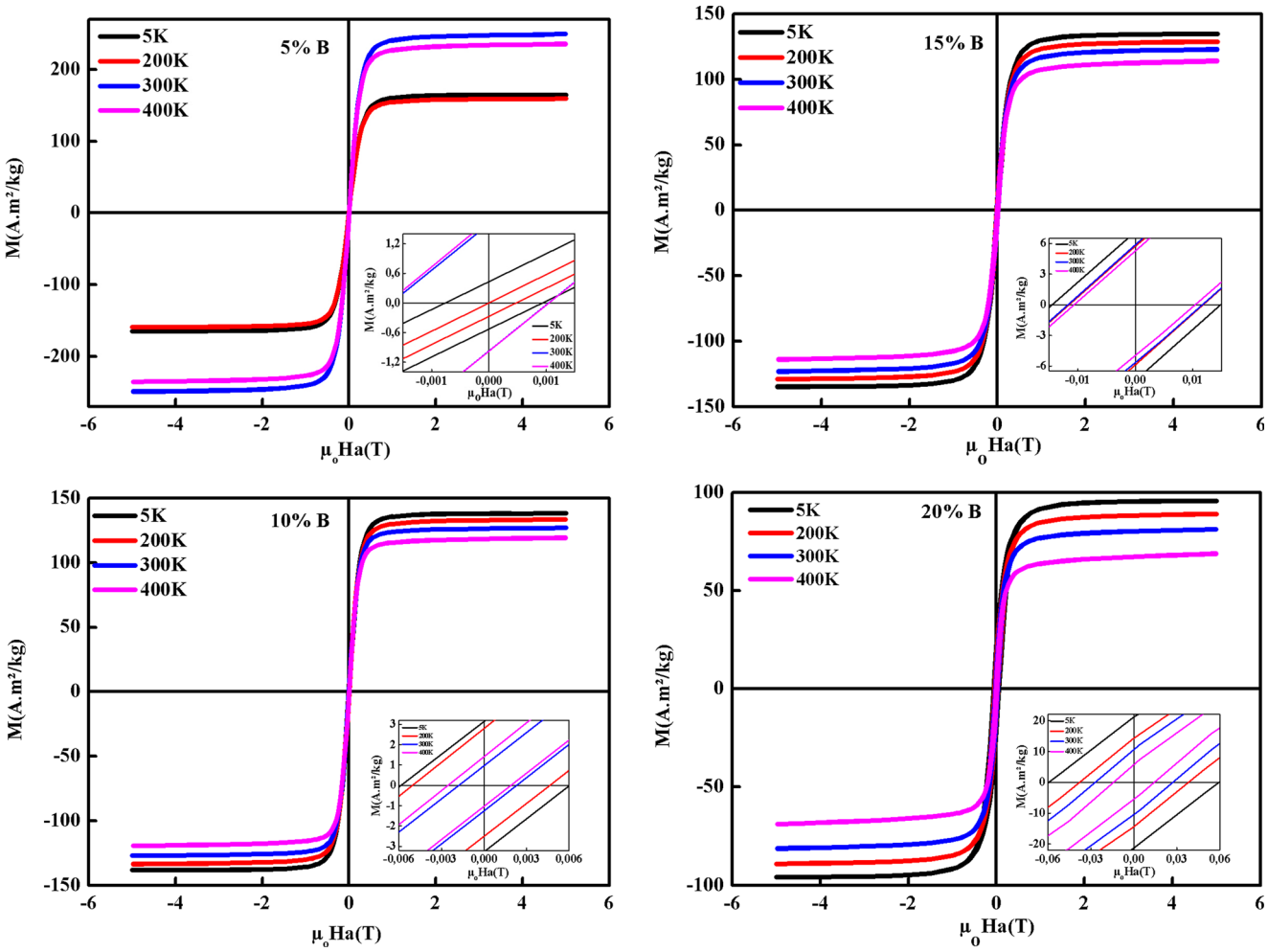

Fig. 3 Hysteresis loops of the $Fe_{92-x}Nb_8B_x$ ($x = 5$, 10, 15, and 20) powders, taken for different temperatures. The inset shows the enlargement of the central part

The lattice parameter of α-Fe is B content independent, while those of the Fe_2B boride phase (a and c) exhibit an antagonistic behavior as a function of B content. Indeed, the lattice parameter a decreases linearly whereas c increases slightly up to 15% B and then rapidly for 20% B. The relative deviations of the lattice parameters a and c are of about $\Delta a = -1\%$ and $\Delta c = 1.82\%$. The lattice distortion which is characterized by lattice expansion and/or contraction can be attributed to the presence of a great quantity of point defects or vacancies inside the nanometer crystallites due to their higher energetic solution.

3.3 Magnetic Properties

The hysteresis loops of the mechanically alloyed $Fe_{92-x}Nb_8B_x$ powders ($M(H)$), taken at different temperatures, are displayed in Fig. 3 as a function of boron content. The insets show the enlargement of the low-field portion of the hysteresis loops. The magnetic properties are dependent on the sample microstructure such as crystallite size, particle morphology, and structural defects. The hysteresis curves display typical soft magnetic characteristics, and the steep augmentation in $M(H)$ near $\mu_0 Ha = 0$ can be due to domain wall movement. Figure 4 reveals that the variation of coercivity (H_c) as a function of B content exhibits the same trend as that of the amorphous phase proportion. Indeed, H_c increases with the augmentation of B content. Furthermore, the magnetic hardening at low temperatures is evidenced by the important increase of coercive field for the 20% B sample from 0.014 to 0.0595 T by lowering the temperature from 400 to 5 K, respectively. The augmentation of H_c might be linked to the presence of small precipitates within the hard magnetic phase. For example, boron is a brittle and hard material, and consequently, boron inclusions remain without mixing in the matrix even after mechanical amorphization of the material. Also, the very small miscibility of Fe, Nb, and B leads to

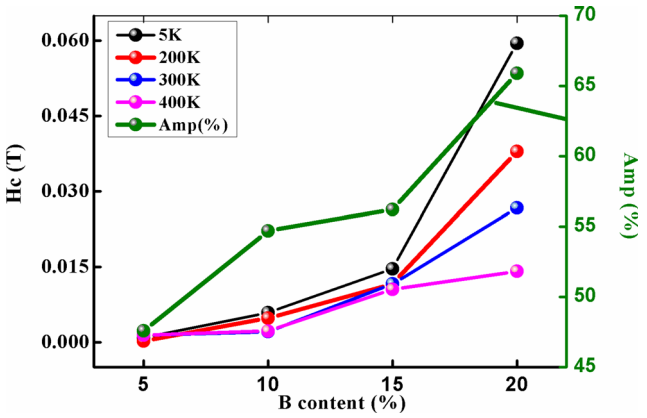

Fig. 4 Variation of coercivity (H_c) and amorphous phase proportion as a function of B content

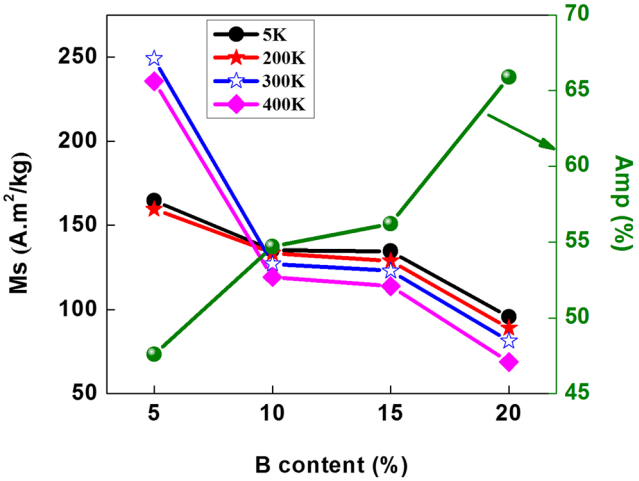

Fig. 5 Evolution of saturation magnetization (M_s) and amorphous phase proportion vs. B content

the presence of unmixed inclusions within the amorphous phase which impede the domain wall movement, leading to the increase of coercivity. Such an assumption can be confirmed by the increase of the amorphous phase-relative proportion as a function of B content. Simultaneously, the saturation magnetization (M_s) decreases with increasing B content as shown in Fig. 5. The drop of M_s might be due to the formation of the hard magnetic phase Fe_2B as well as to the structural disorder which is introduced during the milling process. Consequently, the magnetic moment decreases through the change in the configuration of the nearest neighbors of magnetic Fe atoms via the substitution of Fe atoms by Nb and/or B ones. In fact, the magnetic atomic moment is assumed to depend on the number of magnetic and metalloid atoms in the first nearest-neighbor shell. Therefore, the decrease of M_s can be correlated to the decrease of the coordination of nearest-neighbor magnetic

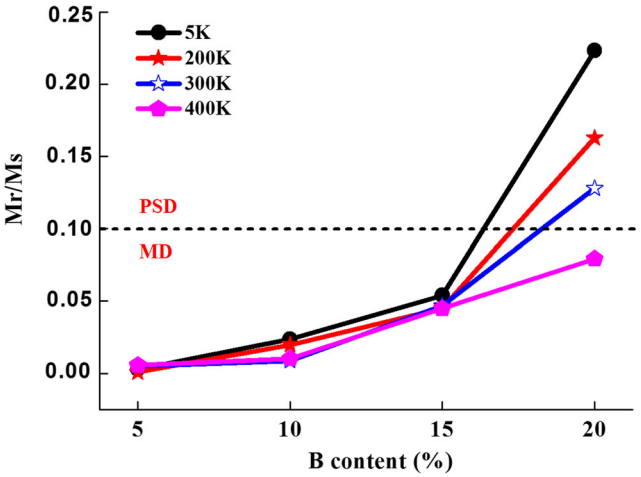

Fig. 6 Changes of squareness ratio (M_r/M_s) against B content

atoms due to the high metalloid content at.% (Nb+B). Comparable results have been reported on the decrease of M_s as the formation of the amorphous phase is accelerated [6]. The remanence-to-saturation ratio (M_r/M_s) is plotted against B content for different temperatures in Fig. 6. By comparing the M_r/M_s values with those of the models based on the displacement of the domain walls [33] and experimental results, 5% B, 10% B, and 15% B samples are multidomains ($M_r/M_s < 0.1$) for all temperatures. Furthermore, the 20% B sample is multidomain for 400 K and pseudo-single domains ($0.1 < M_r/M_s < 0.5$) for 5, 200, and 300 K.

Figure 7 represents the normalized temperature dependence magnetization (M–T) of the $Fe_{92-x}Nb_8B_x$ ($x = 5$, 10, 15, and 20) alloys measured under a magnetic field of 0.05 T in the temperature range of 200–750 K. For lower and higher boron contents, the magnetization curves exhibit different behaviors. In fact, the magnetization shows an increase at about 400 and 670 K for 20% B and 5% B, respectively, that can be attributed to the crystallization of the amorphous phase. On further heating of the 5% B sample beyond 740 K, the decrease of the magnetization to zero can be associated with the ferromagnetic-paramagnetic transition of the α-Fe(Nb, B) solid solution. The effect of the boron content on the composition of the amorphous phase and, therefore, the magnetic transition temperature is evidenced by the thermal derivative of the magnetization with respect to the temperature, dM/dT (Fig. 8). The Curie temperature (T_C) increases with increasing B content up to 15% B and then decreases for 20% B. T_C depends on the exchange interaction between the magnetic moments, which, in turn, depends on the distance between the magnetic atoms. Consequently, T_C depends on the composition of the amorphous structure. Also, the increase of T_C might come from the penetration of the exchange field caused by

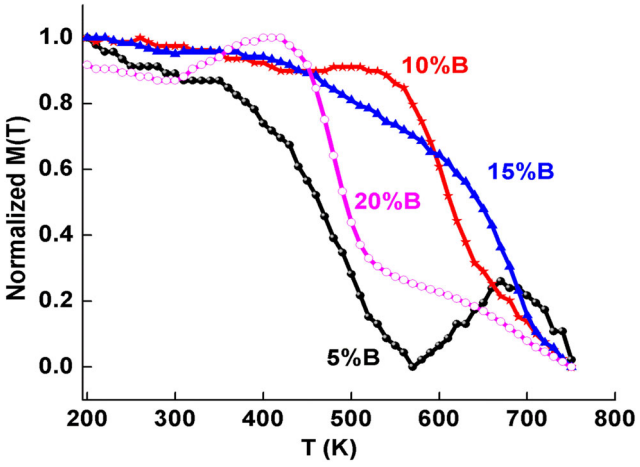

Fig. 7 Temperature dependence magnetization (M–T) of the $Fe_{92-x}Nb_8B_x$ compounds measured under a magnetic field of 0.05 T

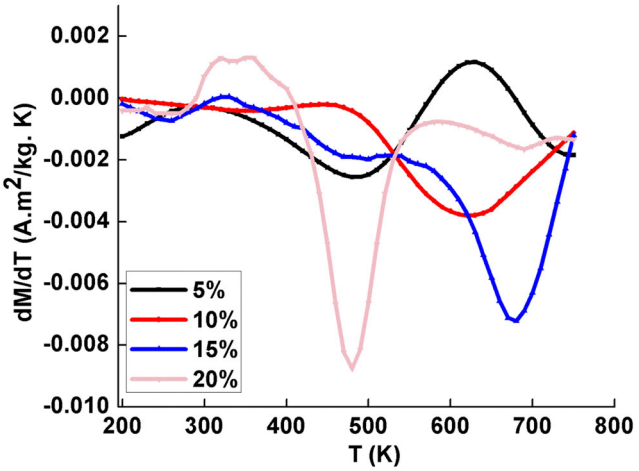

Fig. 8 dM/dT variation as a function of temperature

the NC α-Fe into the residual amorphous matrix [34]. It is well known that B and Nb have different effects on T_C, while B generates strong intergranular magnetic coupling, leading to the increase of T_C, and Nb reduces the intergranular coupling, thereby decreasing T_C. Thus, the increase of T_C might be related to the B effect while its decrease in the case of 20% B can be due to the presence of Nb atoms in the vicinity of Fe ones. It seems that the overall composition of the residual amorphous phase, rather than the unmixed Fe content alone, appears to determine T_C of the milled powders. Also, the broader peaks in dM/dT curves point out the existence of an inhomogeneous atomic order which results in spreading of the local T_C. This can be due to the hardness and brittleness of boron, on the one hand, and its very low solubility in Fe, on the other hand. The broadening of the magnetic transition can be linked to the multiphase character of the mechanically alloyed FeNbB system, the presence of impurity phases such as remnant inclusions [6], or the existence of a distribution of T_C in amorphous phases.

4 Conclusions

$Fe_{92-x}Nb_8B_x$ ($x = 5$, 10, 15, and 20) powder mixtures have been prepared by MA. The end product consists of an amorphous structure, NC α-Fe and Fe_2B phases. FeB boride is observed for 15 and 20% B samples. The crystallite sizes are in the range of 7–24 nm, and the volume fraction of the disordered amorphous phase increases with increasing B content and reaches a maximum value of about 66% for 20% B. As B content increases, H_c increases and M_s decreases. The magnetic hardening is evidenced by the important augmentation of H_c for the 20% B sample from 0.014 to 0.0595 T by lowering the temperature from 400 to 5 K, respectively. T_C of the amorphous phase rises with increasing B content up to 15% B and then decreases.

Funding Information This work was supported by the Algerian Ministère de l'Enseignement Supérieur et de la Recherche Scientifique, the PHC-Maghreb 15 MAG07 program, and the Spanish MINECO projects MAT2013-47231-C2-2-P and MAT2016-75967-P.

References

1. Alleg, S., Ibrir, M., Fenineche, N.E., Azzaza, S., Suñol, J.J.: J. Alloys Compd. **494**, 109–115 (2010)
2. Bensebaa, N., Loudjani, N., Alleg, S., Dekhil, L., Suñol, J.J., Al Sae, M., Bououdina, M.: J. Magn. Magn. Mater. **349**, 51 (2014)
3. Alleg, S., Barker, J.M. (eds.): Powder Engineering, Technology and Applications. Nova Science Publishers Inc, New York (2011)
4. Azzaza, S., Alleg, S., Suñol, J.J.: J. Therm. Anal. Calorim. **119**, 1037–1046 (2015)
5. Bensebaa, N., Alleg, S., Grenèche, J.M.: J. Alloys Compd. **393**, 194–203 (2005)
6. Ipus, J.J., Blázquez, J.S., Conde, C.F., Borrego, J.M., Franco, V., Lozano-Pérez, S., Conde, A.: Intermetallics **49**, 98–105 (2014)
7. Brahimi, A., Alleg, S., Yamkane, Z., Lassri, H., Suñol, J.J., Hlil, E.K.: J. Supercond. Nov. Magn. **30**, 3045 (2017)
8. Alleg, S., Souilah, S., Younes, A., Bensalem, R., Suñol, J.J., Greneche, J.M.: J. Alloys Compd. **536S**, S394–S397 (2012)
9. Souilah, S., Alleg, S., Bououdina, M., Suñol, J.J., Hlil, E.K.: J. Supercond Nov. Magn. **30**, 1927 (2017)
10. Suñol, J.J., Güella, J.M., Bonastrea, J., Alleg, S.: J. Alloys Compd. **483**, 604–607 (2009)
11. Ling-fei, C., Ming-pu, W., Dan, X., Ming-xing, G., Zhou, L., Gen-ying, X.: Trans. Nonferrous Met. Soc. China **16**, 299–303 (2006)
12. Ipus, J.J., Blazquez, J.S., Franco, V., Conde, A., Kiss, L.F.: Intermetallics **18**, 565–568 (2010)
13. Blázquez, J.S., Ipus, J.J., Conde, C.F., Conde, A.: J. Alloys Compd. **615**, S555–S558 (2014)
14. Li, W., Yang, Y.Z., Xu, J., Xie, C.X.: J. Supercond. Nov. Magn. **30**, 1877 (2017)
15. Stoica, M., Hajlaoui, K., Das, J., Eckert, J., Yavari, A.R.: Rev. Adv. Mater. Sci. **18**, 61–65 (2008)
16. Varga, L.K., Bakos, E., Koszó, E.K., Zsoldos, E., Kiss, L.F.: J. Magn. Magn. Mater. **133**, 280 (1994)
17. Balogh, J., Kemény, T., Vincze, I., Budjosó, L., Tóth, L., Vincze, G.: J. Appl. Phys. **77**, 4997 (1995)
18. Alleg, S., Hamouda, A., Bensalem, R., Suñol, J.J., Grenèche, J.M., Azzaza, S.: Mater. Chem. Phys. **122**, 35–40 (2010)
19. Calka, A., Radlinski, A.P.: Mater. Sci. Eng. A **134**, 1350–1353 (1991)
20. Imafuku, M., Sato, S., Koshiba, H., Matsubara, E., Inoue, A.: Scripta Mater. **44**, 2369–2372 (2001)
21. Životský, O., Postava, K., Kraus, L., Jirásková, Y., Juraszek, J., Teillet, J., Barčová, K., Švec, P., Janičkovič, D., Pištora, J.: J. Magn. Magn. Mater. **320**, 1535–1540 (2008)
22. Škorvánek, I., Kováč, J., Marcin, J., Duhaj, P., Gerling, R.: J. Magn. Magn. Mater. **203**, 226–228 (1999)
23. Suñol, J.J., González, A., Saurina, J., Escoda, L., Bruna, P.: Mater. Sci. Eng. A **874-880**, 375–377 (2004)
24. Torrens-serra, J., Bruna, P., Rodriguez-Viejo, J., Roth, S., Clavaguera-Mora, M.T.: Intermetallics **18**, 773–780 (2010)
25. Lutterotti, L.: MAUD version 2.55, http://maud.radiographema.com/
26. Rietveld, H.M.: J. Appl. Cryst. **2**, 65–71 (1969)
27. Blasquez, J.S., Franco, V., Conde, C.F., Conde, A.: Intermetallics **15**, 1351–1360 (2007)
28. Takeuchi, A., Inoue, A.: Mater. Trans. **46**, 2817–2829 (2005)
29. Hasegawa, R., Ray, R.: J. Appl. Phys. **49**, 4174 (1978)
30. Azzaza, S.: Phd Thesis University of Annaba Algeria (2009)
31. Massalski, T.B. Binary Alloy Phase Diagrams, 2nd edn. ASM International, Materials Park, Ohio (1990)
32. Rico, M.M., Grenèche, J.M., Alcazar, G.A.P.: J. Alloys Compd. **398**, 26–32 (2005)
33. Fallot, M.: Masson et Cie (1935)
34. Hernando, A., Amils, X., Nogués, J., Suriñach, S., Baró, M.D., Ibarra, M.R.: Phys. Rev. B **R11**(864), 58 (1998)